ACS APPLIED NANO MATERIALS
Cite This: ACS Appl. Nano Mater. 2019, 2, 3246−3252
Article
www.acsanm.org

Inkjet Printing Multicolor Pixelated Quantum Dots on Graphene for Broadband Photodetection

Brent Cook,*,† Maogang Gong,† Dan Ewing,‡ Matthew Casper,‡ Alex Stramel,‡ Alan Elliot,‡ and Judy Wu*,†

†Department of Physics and Astronomy, University of Kansas, Lawrence, Kansas 66045, United States
‡Department of Energy's National Security Campus, Kansas City, Missouri 64147, United States

Supporting Information

ABSTRACT: Pixelated broadband photoconductors consisting of chemical vapor deposition (CVD) grown graphene on Si/SiO_2 and colloidal ZnO and PbS quantum dots (QDs) and FeS_2 nanocrystals (NCs) are fabricated by inkjet printing of the QDs and NCs onto predefined graphene channels between Au electrodes. For a comparison, tandem devices with multilayers of QDs were also fabricated on graphene. The optoelectronic performance of these devices was characterized at different wavelengths in the ultraviolet−visible−near-infrared spectra. Specifically, the photoresponsivities are 97.5 A/W (24.4 A/W·V), 7.41 A/W (1.85 A/W·V), and 6.81 A/W (1.70 A/W·V) on the ZnO (340 nm), FeS_2 (550 nm), and PbS (900 nm) channels, respectively, which correspond to the external quantum efficiencies (EQE) of 35580%, 1670%, and 940% for the three channels. In addition, the dynamic response of the ZnO-QD/graphene, PbS-QD/graphene, and FeS_2-QD/graphene devices are 2 s/29 s, 300 ms/3.2 s, and 204 ms/240 ms for the rise and fall times, respectively, where the ZnO-QD, PbS-QD, and FeS_2-QD device channels are measured at wavelengths of 340, 900, and 550 nm, respectively, all at a 1.0 V bias. In contrast, the photoresponsivities are 0.67 and 20.8 A/W for 900 and 340 nm, respectively, for the tandem device and with EQE values of 90% and 7590%, in addition to response times of 12.1 and 40.3 s at 900 nm and no appreciable response time to 340 nm. This result shows that the pixelated photoconductor benefits from direct charge transfer to the graphene channel whereas the tandem devices suffer from inefficient charge transfer between different QD layers that reduces the responsivity and response speed. This low-cost printed pixelated QD/graphene device shows the viability of printed broadband photoconductors compared to more expensive routes of device fabrication, in addition to offering compatibility to current standard complementary metal oxide semiconductor devices.

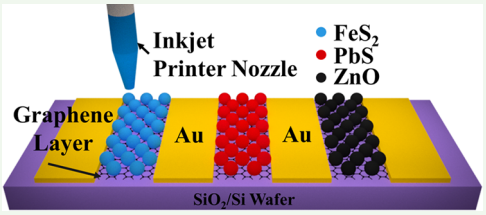

KEYWORDS: *inkjet printing, multiwavelength, quantum dots, photodetector, sensor*

INTRODUCTION

Graphene is a single atomic layer of carbon atoms arranged in a honeycomb-patterned crystal lattice with a superior charge carrier mobility, chemical inertness, ∼97% transparency, and flexibility, making it appealing for a variety of optoelectronic nanodevices.[1−3] However, graphene lacks an electronic bandgap and therefore is incapable of detecting specific wavelengths of light unless combined with other types of photosensitizers such as quantum dots (QDs),[4,5] plasmonics,[6] polymers,[7] or other nanostructures.[8−13] Incorporating these sensitizers often involves methods such as spin-coating, solution-growth, chemical vapor deposition (CVD), physical vapor deposition, and so on, which often require an elevated temperature/harsh environments to form high-quality crystalline sensitizers, which may not be compatible with graphene and/or complementary metal oxide semiconductors (CMOS) used for integrated circuits. Colloidal QDs offer a resolution to these issues as they can be prefabricated at optimal conditions and integrated through inkjet printing or spin-coating on graphene at room temperature. In addition, the QD wavelength selectivity can be tuned by adjusting the QD materials and dimensions, which eliminates the need for color filters in combination with CMOS read-out circuits for image detectors.[9,14−16] For example, ZnO, PbS, and FeS_2 are semiconductors with remarkable performances in detection of the ultraviolet (UV), visible (vis), and near-infrared (NIR) detection, respectively. Utilizing the properties ZnO, PbS, and FeS_2, with bandgaps of ∼3.4, ∼1.2, and ∼0.95 eV, respectively, a broadband nanohybrid photoconductor can be created by printing these QDs on graphene to form QD/graphene van der Waals (vdW) heterojunctions.[17−19] These broadband photodetections have wide applications in telecommunications,[20] UV−IR imaging,[15] photodetection,[21−23] and biosensing.[24,25]

Inkjet printing offers unique advantages in mass scalability, cost reduction, low waste, and direct deposition on targeted regions.[26,27] In particular, inkjet printing allows photonic and high-performance electronic components based on functional nanomaterials and quantum nanostructures prefabricated into

Received: March 22, 2019
Accepted: May 3, 2019
Published: May 3, 2019

DOI: 10.1021/acsanm.9b00539
ACS Appl. Nano Mater. 2019, 2, 3246−3252

highly crystalline structures and desired morphologies to be incorporated with CMOS circuits without the need to address the incompatibility issue of the thermal budgets.[28] Extensive efforts have been put into research of inkjet printing with exciting progress made in the past decade or so.[27−30] Research into how to form well-controlled ink droplets is defined utilizing Weber, Reynolds, and Ohnesorge numbers which characterize droplet formation and must be adjusted to the optimal ranges.[29,31−33] The Weber and Reynolds numbers are defined as $N_W = v^2\rho\alpha/\gamma$ and $N_R = v\rho\alpha/\eta$, respectively, which results in an Ohnesorge number of $N_O = (N_W)^{1/2}/N_R = \eta/(\rho\gamma\alpha)^{1/2}$, where v, ρ, η, γ, and α are the ink's average travel velocity, density, viscosity, surface tension, and the printer head's nozzle diameter.[31−33] The inverse of the Ohnesorge number is the Z parameter that offers the best indicator for printable inks: if $Z < 1$, the ink is too viscous, and if $Z > 10$ it is too fluid. However, we avoid satisfying these requirements by utilizing piezoelectric inkjet dispensing in conjunction with capillary action with very fluid ink and low dispensing voltages, which is described in the Experimental Section.[29,31,32]

In this work, three-color QD/graphene vdW heterojunction photoconductors were fabricated by inkjet printing ZnO QDs, PbS QDs, and FeS_2 NCs inks on each of the three channels of graphene. The goal is to print pixelated broadband photoconductors in comparison to a printed tandem broadband photoconductor. The selectivity of each channel for photodetection in the UV−vis−IR spectra was characterized to illustrate spectral selectivity of the three-pixel devices with each channel acting as a cross-check for different wavelengths. The QDs/graphene photoconductor structure was selected to take advantages of the high charge carrier mobility of graphene and extended exciton lifetime in QDs to provide high photoconductive gain and hence high photoresponsivity.[34] Specifically, the ZnO QDs/graphene vdW heterojunction photodetectors have shown responsivity up to $\sim 10^8$ A/W at a wavelength of 340 nm with an intensity of 2.5 μW/cm^2.[16,35] The PbS QDs/graphene and FeS_2 NCs/graphene channels have also shown high responsivities up to $\sim 10^6$ A/W at wavelengths of 300−600 nm, taking advantage of the high gain in QD/graphene horizontal devices. This is in contrast to graphene/PbS-QDs/graphene sandwich vertical photoconductor case that has shown responsivities up to 1 A/W at a wavelength of 640 nm at an intensity of 430 μW/cm^2.[9,36,37] A comparison with tandem structured ZnO-QD/PbS-QD/graphene devices was also made to illustrate the advantage of the pixelated counterparts in reducing the detrimental effect of the QD−QD junctions in reducing photoresponse and response speed.

EXPERIMENTAL SECTION

The PbS QDs and FeS_2 NCs were synthesized in an argon environment Schlenk line system, and the full experimental steps and synthesizing procedure are described in the Supporting Information. The ZnO QDs were synthesized using a hydrothermal method, and the synthesizing details can also be found in the Supporting Information. Transmission electron microscopy (TEM) and high-resolution TEM (HRTEM) were employed to characterize the crystallinity, morphology, and dimensions of the QDs and NCs. CVD was applied for synthesis of graphene on polycrystalline Cu foils using the same process reported in our previous publications.[38] A wet transfer process was then applied to the graphene/Cu-foil by spin-coating poly(methyl methacrylate) PMMA onto the graphene and dissolving the Cu foil; then the graphene/PMMA was floated in deionized (DI) water for cleaning and then transferred to SiO_2/Si substrates with Au electrodes. The details of this wet transfer process have been reported previously.[13] The SiO_2/Si substrates were thoroughly cleaned with a acetone, isopropanol, and DI water prior to Au deposition and transferring of graphene. The electrodes were fabricated using standard photolithography followed with e-beam evaporation of Au (40 nm)/Ti (5 nm). The QDs/NCs are mixed into chloroform, which is the medium for the ink. The inkjet printer used is a SonoPlot Microplotter Proto, which is operated with the SonoGuide and SonoDraw software provided. The inkjet printer has spraying and dispensing functionality; however, in our instance capillary action is the main driving force for the inkjet printing. This is achieved by having the inkjet nozzle kept at an ~20 μm distance above the surface of the substrate to maintain a steady stream of ink. The inkjet nozzle, composed of a glass capillary attached to an ultrasonicating piezoelectric device, was used to store and dispense ink drops during the inkjet printing. Depending on the glass tip length, tip diameter, and the amount of ink in the glass capillaries, the piezoelectric dispensing voltage was varied in the range of 1−3 V for controlling a continuous ejection of ink with tip diameter of 136.7 ± 20.8 μm and capillary length of 20.6 ± 0.7 mm. The graphene channel has channel dimensions of 0.3 mm (length) × 3.0 mm (width) between the two Au electrodes. The larger graphene channel size allows us to avoid lithography of graphene for a smaller channel that can potentially incorporate contaminates that can dirty the graphene surface with photo- and e-beam resist, developers, and etchants. The number of printed scans was in the range of 10−20 to ensure uniform coverage of the graphene channel. After the PbS QDs and FeS_2 NCs were printed, 3-mercaptopropionic acid (MPA) ligand exchange was performed for QD (or NC) surface passivation and for facilitating charge transfer from QD (or NC) to graphene; this is important for PbS and FeS_2 specifically because they are synthesized using organic solutions (see details in the Supporting Information).[9] The ligand exchange is unnecessary for ZnO QDs since the fabrication process is largely inorganic solutions.[16] Optical microscopy and scanning electron microscopy (SEM, JEOL JSM-6380) images were taken for the analysis of the sample morphology. Optical absorption spectra were taken to confirm the bandgap and QDs and NCs. For optoelectronic characterization, a CHI660D electrochemical station together with a Newport Oriel Apex monochromator with an Oriel Cornerstone 130 1/8 m monochromator filter was used to measure the current−voltage characteristic in the dark and under illumination, dynamic, and spectral photoresponse.

RESULTS AND DISCUSSION

Figure 1 depicts schematically the three-pixelated photodetectors by printing three different kinds of QDs and NCs on the graphene channels. Specifically, three different nozzles containing ZnO QDs (black), PbS QDs (blue), and FeS_2 (red) NCs were employed for printing each of them on the different

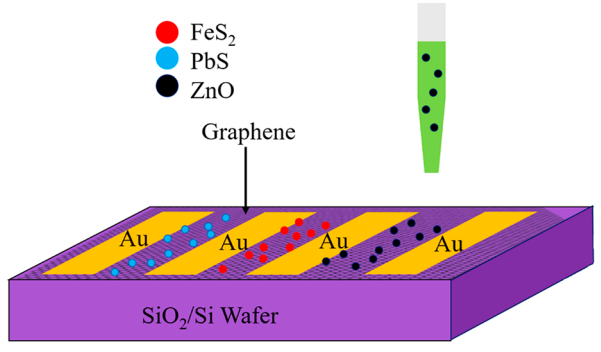

Figure 1. Schematic diagram of printing of ZnO QDs (black), PbS QDs (blue), and FeS_2 (red) NCs on graphene channels defined between two nearest-neighbor Au electrodes on SiO_2 (500 nm)/Si substrates.

DOI: 10.1021/acsanm.9b00539
ACS Appl. Nano Mater. 2019, 2, 3246−3252

graphene channels as illustrated in Figure 1. The thickness of the printed QD or NC layer was controlled by adjusting the number of printing scans performed. For ZnO QDs and PbS QDs of comparable QD dimensions and ink concentrations, 10 printing scans were performed to obtain the layer thickness. Considering the FeS_2 NCs have a larger dimensions, they tend to diffuse into the ligand solutions during ligand exchange process, which is likely due to the loose packing of larger nanocrystals; as a result, 20 printing scans were performed for FeS_2 NC. The thicknesses of the printed ZnO, PbS, and FeS layers are approximately 0.30 ± 0.29, 0.57 ± 0.37, and 0.34 ± 0.42 μm, respectively.

The absorption spectra of the three kinds of photosensitizers are shown in Figure 2a along with their TEM images for ZnO

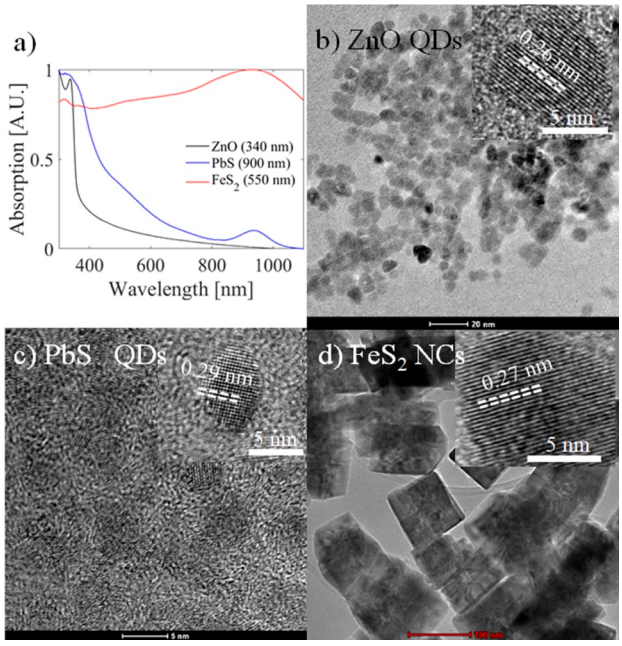

Figure 2. (a) Optical absorption spectra of ZnO QDs (black), PbS QDs (blue), and FeS_2 NCs (red). TEM images of the (b) ZnO QDs, (c) PbS QDs, and (d) FeS_2 NCs with their HRTEM images as the insets.

QDs, PbS QDs, and FeS_2 NCs in Figures 2b, 2c, and 2d, respectively. The ZnO QDs (black) show an absorption edge at ~360 nm as expected from around the energy bandgap of 3.37 eV (Figure 2a). For the PbS QDs (blue), the absorption edge is at around 940 nm, indicating a bandgap of ~1.3 eV, which is in agreement with PbS QDs of size 4 nm (Figure 2a).[18] Lastly, the FeS_2 NCs (red) has a broadband absorption with a broad peak located around 900 nm due to shape-induced localized surface plasmonic resonance as shown in our previous work (Figure 2a).[37] From the TEM images, it is clearly seen that the ZnO and PbS QDs have spherical or irregular shapes while the FeS_2 NCs have a cubic shape. In addition, the average dimensions are approximately 5.6 ± 4.0, 4.3 ± 4.4, and 99.4 ± 19.8 nm for the ZnO QDs, PbS QDs, and FeS_2 NCs, respectively. The insets of Figures 2b, 2c, and 2d, are the HRTEM of the corresponding QDs or NCs, illustrating high crystallinity for the three types of samples. Based on the HRTEM images, the lattice spacings of 0.26, 0.29, and 0.27 nm are observed as expected for ZnO, PbS, and FeS_2, respectively.

The optoelectronic properties of the three-pixelated photoconductors were tested at wavelengths of 340, 550, and 900 nm, respectively. The dynamic photoresponses on the different channels are depicted in Figure 3. The dynamic photoresponse

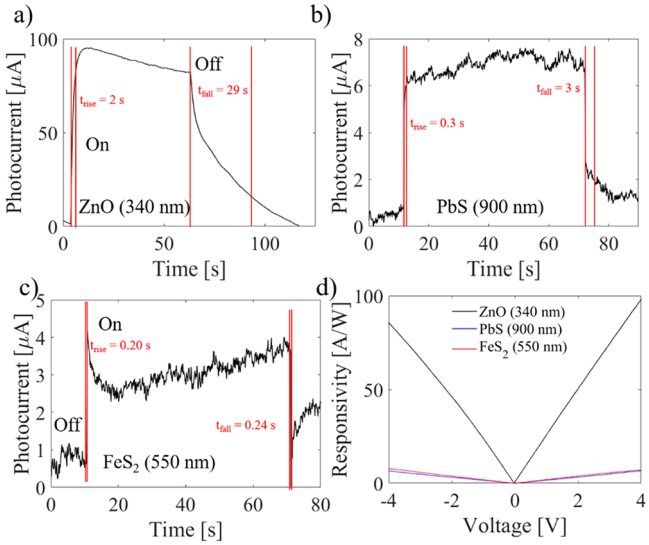

Figure 3. Dynamic photoresponse to light "on" and "off" on (a) ZnO-QD/graphene, (b) PbS-QD/graphene, and (c) FeS_2-NC/graphene photoconductor channels. (d) Photocurrents as a function of the bias voltage in the three channels.

of the ZnO-QD/graphene channel is measured at a 1.0 V bias and 340 nm wavelength (Figure 3a). The rise and fall times are defined as the time for the photocurrent to rise from 0% to 80% and decay from 100% to 20% of the maximum photocurrent, respectively. It should be noted that different definitions of the rise and fall times, such as 0−50% for rising time and 100%−50% for the falling time, have also been used in the literature.[16,39] If we would use the 0%−50% and 100%−50% definition for the time constants, we would obtain rise/fall times of approximately 100 ms/50 ms, 60 ms/140 ms, and 900 ms/9.4 s for the FeS_2-QD/graphene, PbS QDs/graphene, and ZnO QDs/graphene single channel devices. These time constants are a half to an order of magnitude smaller than that obtained using the 0%−80% and 100%−20% definitions for the rise and fall times, respectively. Considering both definitions have been conventions utilized to obtain time constants, they will be used in this paper where the time constants estimated by using the rising from 0%−80% and falling from 100%−20% definition will be reported with no parentheses and the values from the other definition in parentheses. By use of these two conventions, the rise and fall times of the ZnO-QD/graphene channel are 2 s (900 ms) and 29 s (9.4 s), respectively. This result is comparable and slightly better than previously reported single-channel ZnO-QDs/graphene devices with 5 and 85.1 s for the rise and fall times, respectively, which is likely the result of longer aging of the ZnO-QDs while kept in storage.[16] However, the response of ZnO-QDs/graphene channel is considerably slower than the PbS-QD/graphene and FeS_2-NC/graphene channels most probably due to the MPA ligand exchange that passivates the surface of the PbS-QD and FeS_2-NC and the interfaces of the QD−QD junctions as well as the PbS-QD/graphene and FeS_2-NC/graphene heterojunctions to eliminate/reduce the charge traps.[9,16,37] Specifically, the rise and fall time constants of the

DOI: 10.1021/acsanm.9b00539
ACS Appl. Nano Mater. 2019, 2, 3246−3252

PbS-QD/graphene channel are 0.3 s (60 ms) and 3.2 s (140 ms) at a 1.0 V bias at 900 nm illumination (Figure 3b). In fact, similar rise and fall times of 0.01−0.26 s and 1−1.7 s, respectively, have been reported previously on PbS/graphene photodetectors.[34,40] In addition, ZnO-QD/graphene (Figure 3a) and PbS-QD/graphene (Figure 3b) show a asymmetric rise and fall in dynamic response, indicating other processes such as charge traps, which indicate that there is a room for improvement via eliminating charge traps. Interestingly, the FeS_2-NC/graphene channel approximately has a symmetric rise and fall time of 0.20 s (100 ms) and 0.24 s (50 ms) at 1.0 V bias at a wavelength of 550 nm (Figure 3c). Furthermore, the printed FeS-NC/graphene channel shows better results than previous work which demonstrated a rise/fall time of 0.6 s/7.6 s, respectively.[37] The considerably shorter response times in PbS-QD/graphene and FeS_2-NC/graphene channels as compared to the ZnO-QD/graphene counterpart may be attributed to the MPA ligand exchange applied to the former cases, which reduces the charge traps at the surface defects of the sensitizers (QD and NC) and the QD−QD (or NC−NC) and QD (or NC)/graphene junctions, whereas ZnO has oxygen absorption and desorption, which contributes to the rise and fall time by electron localization and delocalization.[9,37]

The photoresponsivity used to characterize the different channels is defined as the photocurrent I_{ph} divided by the power of the incident light (P), where $I_{ph} = I_{light} - I_{dark}$, and so $R = I_{ph}/P$ and the external quantum efficiency (EQE) can be calculated from responsivity and is given by EQE = Rhf/e, where h is Planck's constant, f, is the frequency of the light, and e is the elementary charge. The channels also show a linear trend of R with a varying voltage bias as shown in Figure 3d, with a photoresponsivity of 7.41 A/W (1.85 A/W·V) for the FeS_2−NC/graphene channel measured with a wavelength of 550 nm and a power of 18.1 μW and with an EQE value of 1670%. Similarly, the PbS-QD/graphene channel has a photoresponsivity of 6.81 A/W (1.70 A/W·V) and an EQE of 940% at a wavelength of 900 nm at a power of 27.5 μW. Finally, the ZnO-QDs/graphene channel has a photoresponsivity of 97.5 A/W (24.4 A/W·V) at a wavelength of 340 nm and a power of 6.66 μW and with an external quantum efficiency (EQE) value of 35580%. The large EQE in exceeding 100% can be attributed to photoconductive gain in the QDs/graphene photoconductive photodetectors.[34,41] In these devices, large photoconductive gains up to 10^8 have been demonstrated due to the combination of the strong quantum confinement in QDs and high charge mobility in graphene.[34,41] The former leads to long lifetime ($\tau_{exciton}$) of excitons or electron−hole pairs and hence the trapped charges (after the transfer of the other type of charges to graphene) in the QDs. The latter facilitates short transit time of charges ($\tau_{transit}$) between the source an drain electrodes. Considering the photoconductive gain is proportional to the ratio of the two time constants $\tau_{exciton}/\tau_{transit}$ that can be as high as 10^8 in QD/graphene devices, EQE ≫ 100% can be obtained. This means that the effective charges detected in the graphene layer can exceed one charge per photon.[34,41] The performance of the PbS-QDs/graphene device is comparable to the previous report of ∼8.4 A/W with similar graphene channel dimensions.[41] However, the ZnO-QDs/graphene channel has significantly improved performance than previously reported (∼0.5 A/W).[35] Furthermore, the high performance of the inkjet printed FeS_2 NC on graphene represents the first report with a graphene channel length of a few hundred micrometers. Considering a shorter graphene channel would lead to higher photoconductive gain and hence higher photoresponsivity as shown in the previous works on the FeS_2-NC/graphene, PbS-QDs/graphene, and ZnO-QDs/graphene[9,16,34,37,40] means further improvement can be obtained on the printed pixelated QD/graphene photoconductors through optimization of the graphene channel.

The photoresponsivity as a function of the light power is depicted at wavelengths of 340, 550, and 900 nm (Figures 4a, 4b, and 4c) at a 1.0 V bias, and the normalized spectral curve is depicted in Figure 4d. Only ZnO/graphene and PbS/graphene is measured for 340 nm; FeS_2 was also measured but displayed a poor dynamic response to UV light and so was not included. Similarly, ZnO mainly shows noise in wavelengths larger than ∼380 nm and was not included in the measurements for 550 and 900 nm. ZnO shows a photoresponsivity inversely related to the power and is comparable to the measured photoresponsivity of from the photocurrent−voltage characteristics curve, which gives ∼24.4 A/W for 1.0 V bias. Similarly, PbS QDs also show an inversely related trend at all wavelengths; however, the photoresponsivity is about as half as much in this measurement as compared to what was measured from the current−voltage characteristic curve. This is likely caused by some degradation attributed to some oxidation of the PbS particles, and similar behavior is seen in FeS_2. Looking at the spectral curves, they show that the ZnO QDs has a band edge at ∼360 nm, while PbS QDs and FeS_2 NCs are broadband nanomaterials that absorb light at all wavelengths. In addition, the spectral curve shows a similar broad peak for FeS_2 around 800 nm with a steady decrease as seen in previous work.[37] For PbS there is a similar small peak slightly shifted to the right of FeS_2 and then an increase in UV absorption, while ZnO has no absorption then begins absorption around 380 nm.[9,16] It should be noted that it is important to evaluate the device performance of the inkjet-printed pixelated and tandem photodetectors from the same types of the QDs and also compare with the similar devices fabricated using conventional methods, such as vacuum-based deposition and spin-coating. Moreover, considering the QD−QD junctions will form in printed QDs, the effect of these junctions on the device performance is particularly relevant to design of broadband

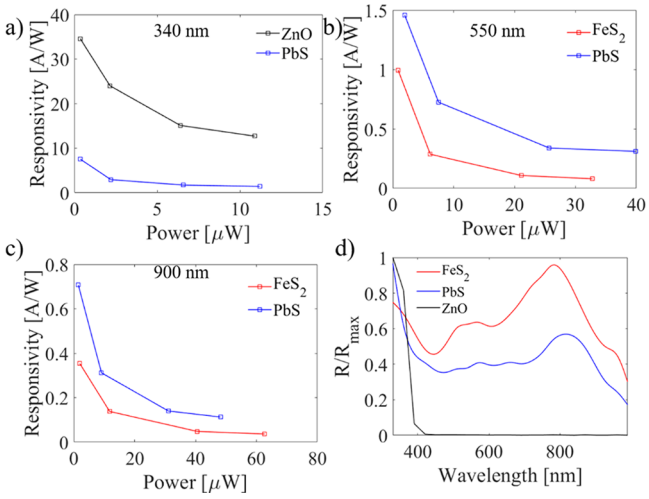

Figure 4. Photoresponsivity as a function of power is depicted in (a), (b), and (c) along with the normalized spectral curve shown in (d).

DOI: 10.1021/acsanm.9b00539
ACS Appl. Nano Mater. 2019, 2, 3246−3252

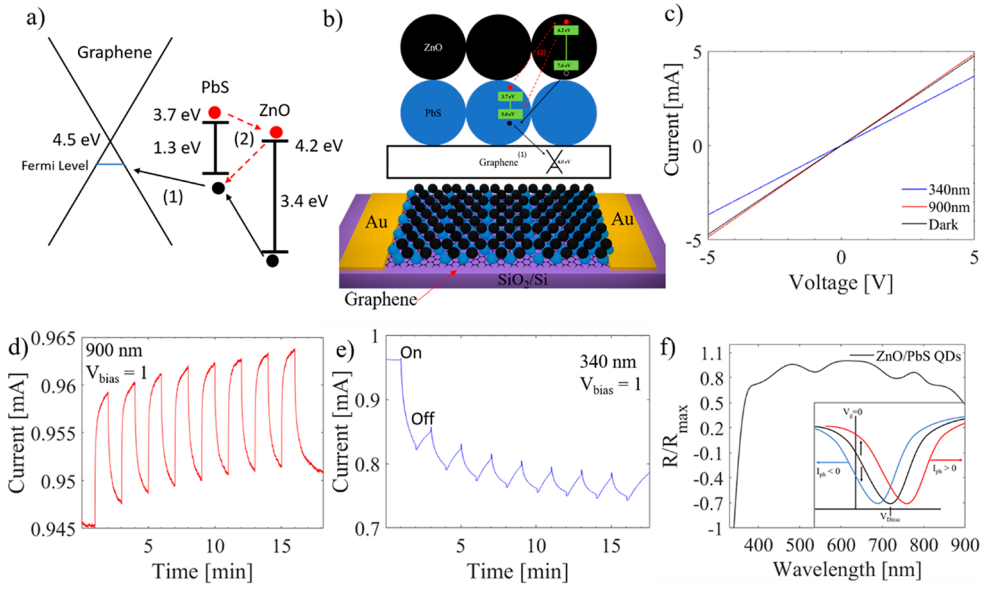

Figure 5. (a) Energy band edge diagram of a ZnO/PbS/graphene tandem structure and a graphic shown in (b). In (c) are the current−voltage characteristic curves, (d) dynamic response to 900 nm, (e) 340 nm, and (f) spectral photoresponse of the tandem device from 330−900 nm. Inset of (f): positive photoresponse (from black to red curve) at a longer wavelength illumination when only PbS-QD layer is active and negative photoresponse at shorter wavelength (blue curve) illumination when both ZnO-QD and PbS-QD layers are active.

photodetectors that may involve QDs of different colors of spectra (or different bandgaps). This evaluation of printed pixelated and tandem structured photodetectors of QDs of different colors would provide critical information to design of broadband photodetectors that may outperform their counterparts made using conventional approaches.

In addition, the tandem device structure shown in Figure 5 is a multilayer QD vdW nanohybrid structure, which differs from conventional tandem photovoltaics based on p−n junctions. Moreover, the band-edge alignment shown in Figure 5a facilitates exciton dissociation and charge transfer through vdW heterojunction of ZnO-QDs/PbS-QDs/graphene from the larger bandgap ZnO-QD top layer to the lower bandgap PbS-QD bottom layer and then to graphene. These vdW heterojunctions have shown to be equally efficient as demonstrated in many vdW heterojunction-based optoelectronics.[42] However, a major obstacle in the vdW heterostructure optoelectronics is in controlling the vdW interface to eliminate any unwanted interface contaminants. In the ZnO-QDs/PbS-QDs/graphene tandem devices we investigate in this work, the controlling of the QD−QD junctions is one such example and should be addressed in future research for optimal performance of this kind of tandem device. Both physical and chemical methods may be promising to address the QD−QD junction issue. For example, an ultrafast thermal annealing (UTA) was found to generate nanoscale junctions between oxide nanoparticles and improves the electron transport properties.[43] On the other hand, certain ligands such as mercaptopropionic acid (MPA) have been found to improve the QD−graphene vdW junctions, resulting improved photoresponse and shortened response time by orders of magnitude.[44] For our ZnO-QDs/PbS-QDs/graphene tandem photodetector shown schematically in Figures 5b, we see through the energy diagram in Figure 5a that the wide-bandgap energy of ZnO will allow lower energy photons to pass through and allow the PbS layer to collect the incident photons, and ZnO and PbS QDs can both absorb high energy photons. However, because of the stacking of QD layers shown in Figure 5b, charges cannot move to the graphene layer from the ZnO QD layer without passing through the PbS QD layer (Figure 5a,b); this can result in an increase dynamic response time. In Figure 5c under 900 and 340 nm we see dramatically different response with a positive photocurrent in the former and a negative photocurrent in the latter. In addition, the dynamic response at 900 nm is slower than in the single QD (or NC)/graphene devices with the rise and fall times respectively being increased up to 12.1 s (3.0 s) and 40.3 s (4.8 s) (Figure 5d). This slower photoresponse may be attributed to the increased number of QD (or NC) layers since photocarriers formed on the top of the QD (or NC) layers must travel across multiple QD−QD junctions before reaching the graphene channel as well as surface defects on QDs (or NCs) would result in charge traps at the QD−QD junctions and slow down the response. In Figure 5e is the response to 340 nm light, and there is no appreciable rise or fall times to the curve and exhibiting a negative photocurrent response. Lastly, a spectral responsivity from 330 to 900 nm wavelengths is shown in Figure 5f. Interestingly, the variation of the responsivity is moderate due to complementary bandgaps of ZnO and PbS QDs despite an overall lower responsivity and slower photoresponse as discussed above. This means the tandem devices can be promising for broadband photodetection if the QD−QD junctions can be improved to optimize the charge transfer and minimize charge trapping. The differences in response could be attributed to a shift in Dirac voltage of graphene. Depicted in Figure 5f is the spectral response, and the inset is a schematic of the Dirac voltage shift. As shown, a positive photoresponse can be seen at longer wavelengths from visible to infrared while a negative photoresponse is shown in the UV spectrum. This means the charges trapped in the PbS-QD layer under longer wavelength illumination are electrons since holes will transfer to graphene, providing a negative gate[9] which lowers the graphene Fermi energy away from the Dirac point (red curve

DOI: 10.1021/acsanm.9b00539
ACS Appl. Nano Mater. 2019, 2, 3246−3252

in the inset in Figure 5f). In the UV spectrum, both PbS-QD and ZnO-QD layers are active, and a transition from positive to negative photoresponse occurs at about 355 nm. This may result from mobile electrons in the ZnO QDs[16] recombining with the holes in the PbS-QD layer (red dashed lines in Figure 5a,b), preventing holes from transferring to graphene. In addition, the electrons in the PbS-QD layer may transfer to the now empty energy states in the ZnO conduction band, and holes can move to the valence band of the PbS-QD layer, resulting in more holes being trapped in the ZnO/PbS film and hence a positive gating of the graphene layer (blue curve inset in Figure 5f). The photoresponsivity at the different wavelengths of the tandem structure at 900 and 340 nm illumination was 0.67 and 20.8 A/W at 55 and 10.9 μW, respectively, with EQE values of 90% and 7590%. The poorer performance of the tandem structure can be contributed to the poor interface between QDs caused by oxidation and ligands at the interface. This poor interface results in lower photoresponsivity and slow dynamic performance. In addition, the alignment of the ZnO and PbS energy bands results in strange behavior due to the proposed dynamic charge exchange between the different active and inactive layers of the ZnO QDs and PbS QDs.

CONCLUSION

In this work, a pixelated broadband photoconductor was printed using inkjet printing onto wet-transferred CVD grown graphene, and a tandem photoconductor is also fabricated. The inkjet printing method has advantages of low material waste and scalability for commercial applications. In particular, it allows direct integration of colloidal QDs and NCs to graphene to form vdW heterostructures for a broad spectrum optoelectronics and sensor devices. In a comparison of pixelated and tandem multicolor photodetectors both fabricated using inkjet printing, we have found that the former has the unique advantages of both faster photoresponse times and larger photoresponsivities, which can be attributed to a direct interface with graphene and the QD layer while the tandem structure creates multiple QD layers that result in charge transfer blocking or/and trapping at the interface of the QD−QD layers as well as to the graphene. The performance of these devices is tested at 340, 550, and 900 nm. It is found that FeS_2/graphene channel has a rise and fall time of 204 and 240 ms, respectively, and a photoresponsivity of 7.41 A/W (1.85 A/W·V) at 4.0 V bias when measured at a wavelength of 550 nm. Similarly, at a wavelength of 900 nm PbS/graphene demonstrated a rise and fall time of 300 ms and 3.2 s and a photoresponsivity of 6.81 A/W (1.70 A/W·V) at 4.0 V bias. Lastly, at 340 nm ZnO shows a performance of 2.0 and 29 s for rise and fall times, respectively, with a photoresponsivity of 97.5 A/W (24.4 A/W·V) at 4.0 V bias. In contrast to the pixelated device, the tandem structure demonstrated an increased rise and fall time of 12.1 and 40.3 s 900 nm and no appreciable rise and fall time to 340 nm. The photoresponsivity was also reduced to 0.67 and 20.8 A/W at 55 and 10.9 μW for 900 and 340 nm, respectively. This shows the viability in an inkjet-printed pixelated broadband photoconductor as opposed to the tandem structure with large possible ability for improvement and selectivity in the UV, visible, and IR range.

ASSOCIATED CONTENT

Supporting Information

The Supporting Information is available free of charge on the ACS Publications website at DOI: 10.1021/acsanm.9b00539.

Experimental synthesizing procedures (PDF)

AUTHOR INFORMATION

Corresponding Authors

*E-mail: bkcook@ku.edu (B.C.).

*E-mail: jwu@ku.edu (J.W.).

ORCID

Brent Cook: 0000-0001-9288-7267

Notes

The authors declare no competing financial interest.

ACKNOWLEDGMENTS

This research was supported by Plant Directed Research and Development funds from the Department of Energy's National Security Campus, operated and managed by Honeywell Federal Manufacturing and Technologies, LLC, under Contract DE-NA0002839. The authors also acknowledge support in part by ARO Contract W911NF-16-1-0029 and NSF Contracts NSF-DMR-1508494 and NSF-ECCS-1809293/1809284.

REFERENCES

(1) Reddy, D.; Register, L. F.; Carpenter, G. D.; Banerjee, S. K. Graphene Field-Effect Transistors. *J. Phys. D: Appl. Phys.* **2012**, *45*, 019501.

(2) Geim, A. K.; Novoselov, K. S. The Rise of Graphene. *Nat. Mater.* **2007**, *6*, 183−191.

(3) Peres, N. M. The Transport Properties of Graphene. *J. Phys.: Condens. Matter* **2009**, *21*, 323201.

(4) Huang, Y. Q.; Zhu, R. J.; Kang, N.; Du, J.; Xu, H. Q. Photoelectrical Response of Hybrid Graphene-PbS Quantum Dot Devices. *Appl. Phys. Lett.* **2013**, *103*, 143119.

(5) Gupta Chatterjee, S.; Chatterjee, S.; Ray, A. K.; Chakraborty, A. K. Graphene−Metal Oxide Nanohybrids for Toxic Gas Sensor: A Review. *Sens. Actuators, B* **2015**, *221*, 1170−1181.

(6) Kim, M.; Kang, P.; Leem, J.; Nam, S. A Stretchable Crumpled Graphene Photodetector with Plasmonically Enhanced Photoresponsivity. *Nanoscale* **2017**, *9*, 4058−4065.

(7) Santra, S.; Hu, G.; Howe, R. C.; De Luca, A.; Ali, S. Z.; Udrea, F.; Gardner, J. W.; Ray, S. K.; Guha, P. K.; Hasan, T. CMOS Integration of Inkjet-Printed Graphene for Humidity Sensing. *Sci. Rep.* **2015**, *5*, 17374.

(8) Tetsuka, H. 2D/0D Graphene Hybrids for Visible-Blind Flexible UV Photodetectors. *Sci. Rep.* **2017**, *7*, 5544.

(9) Gong, M.; Liu, Q.; Goul, R.; Ewing, D.; Casper, M.; Stramel, A.; Elliot, A.; Wu, J. Z. Printable Nanocomposite FeS_2-PbS Nanocrystals/Graphene Heterojunction Photodetectors for Broadband Photodetection. *ACS Appl. Mater. Interfaces* **2017**, *9*, 27801−27808.

(10) Tetsuka, H.; Nagoya, A.; Tamura, S. I. Graphene/Nitrogen-Functionalized Graphene Quantum Dot Hybrid Broadband Photodetectors with a Buffer Layer of Boron Nitride Nanosheets. *Nanoscale* **2016**, *8*, 19677−19683.

(11) Xie, C.; Yan, F. Perovskite/Poly(3-hexylthiophene)/Graphene Multiheterojunction Phototransistors with Ultrahigh Gain in Broadband Wavelength Region. *ACS Appl. Mater. Interfaces* **2017**, *9*, 1569−1576.

(12) Yang, F.; Cong, H.; Yu, K.; Zhou, L.; Wang, N.; Liu, Z.; Li, C.; Wang, Q.; Cheng, B. Ultrathin Broadband Germanium-Graphene Hybrid Photodetector with High Performance. *ACS Appl. Mater. Interfaces* **2017**, *9*, 13422−13429.

(13) Cook, B.; Liu, Q.; Liu, J.; Gong, M.; Ewing, D.; Casper, M.; Stramel, A.; Wu, J. Facile Zinc Oxide Nanowire Growth on Graphene via a Hydrothermal Floating Method: Towards Debye Length Radius Nanowires for Ultraviolet Photodetection. *J. Mater. Chem. C* **2017**, *5*, 10087−10093.
(14) García de Arquer, F. P.; Armin, A.; Meredith, P.; Sargent, E. H. Solution-Processed Semiconductors for Next-Generation Photodetectors. *Nat. Rev. Mater.* **2017**, *2*, 16100.
(15) Goossens, S.; Navickaite, G.; Monasterio, C.; Gupta, S.; Piqueras, J. J.; Pérez, R.; Burwell, G.; Nikitskiy, I.; Lasanta, T.; Galán, T.; Puma, E.; Centeno, A.; Pesquera, A.; Zurutuza, A.; Konstantatos, G.; Koppens, F. Broadband Image Sensor Array based on Graphene−CMOS Integration. *Nat. Photonics* **2017**, *11*, 366−371.
(16) Gong, M.; Liu, Q.; Cook, B.; Kattel, B.; Wang, T.; Chan, W. L.; Ewing, D.; Casper, M.; Stramel, A.; Wu, J. Z. All-Printable ZnO Quantum Dots/Graphene van der Waals Heterostructures for Ultrasensitive Detection of Ultraviolet Light. *ACS Nano* **2017**, *11*, 4114−4123.
(17) Janotti, A.; Van de Walle, C. G. Fundamentals of Zinc Oxide as a Semiconductor. *Rep. Prog. Phys.* **2009**, *72*, 126501.
(18) Moreels, I.; Lambert, K.; Smeets, D.; De Muynck, D.; Nollet, T.; Martins, J. C.; Vanhaecke, F.; Vantomme, A.; Delerue, C.; Allan, G.; Hens, Z. Size-Dependent Optical Properties of Colloidal PbS Quantum Dots. *ACS Nano* **2009**, *3*, 3023−3030.
(19) Yu, B. B.; Zhang, X.; Jiang, Y.; Liu, J.; Gu, L.; Hu, J. S.; Wan, L. J. Solvent-Induced Oriented Attachment Growth of Air-Stable Phase-Pure Pyrite FeS_2 Nanocrystals. *J. Am. Chem. Soc.* **2015**, *137*, 2211−2214.
(20) Zhuge, F.; Zheng, Z.; Luo, P.; Lv, L.; Huang, Y.; Li, H.; Zhai, T. Nanostructured Materials and Architectures for Advanced Infrared Photodetection. *Sci. Technol. Adv. Mater.* **2017**, *2*, 1700005.
(21) Zhang, B. Y.; Liu, T.; Meng, B.; Li, X.; Liang, G.; Hu, X.; Wang, Q. J. Broadband High Photoresponse from Pure Monolayer Graphene Photodetector. *Nat. Commun.* **2013**, *4*, 1811.
(22) Gao, L.; Chen, C.; Zeng, K.; Ge, C.; Yang, D.; Song, H.; Tang, J. Broadband, Sensitive and Spectrally Distinctive SnS_2 Nanosheet/PbS Colloidal Quantum Dot Hybrid Photodetector. *Light: Sci. Appl.* **2016**, *5*, e16126−e16126.
(23) Zheng, Z.; Zhang, T.; Yao, J.; Zhang, Y.; Xu, J.; Yang, G. Flexible, Transparent and Ultra-Broadband Photodetector Based on Large-Area WSe_2 Film for Wearable Devices. *Nanotechnology* **2016**, *27*, 225501.
(24) Hossain, R. F.; Deaguero, I. G.; Boland, T.; Kaul, A. B. Biocompatible, Large-Format, Inkjet Printed Heterostructure MoS_2-Graphene Photodetectors on Conformable Substrates. *NPJ. 2D Mater. Appl.* **2017**, *1*, 28.
(25) Kim, Y. K.; Na, H. K.; Kim, S.; Jang, H.; Chang, S. J.; Min, D. H. One-Pot Synthesis of Multifunctional Au@Graphene Oxide Nanocolloid Core@Shell Nanoparticles for Raman Bioimaging, Photothermal, and Photodynamic Therapy. *Small* **2015**, *11*, 2527−2535.
(26) Singh, M.; Haverinen, H. M.; Dhagat, P.; Jabbour, G. E. Inkjet Printing-Process and its Applications. *Adv. Mater.* **2010**, *22*, 673−685.
(27) Habas, S. E.; Platt, H. S. A.; van Hest, M. F. A. M.; Ginley, D. S. Low-Cost Inorganic Solar Cells: From Ink to Printed Devices. *Chem. Rev.* **2010**, *110*, 6571−6594.
(28) Pace, G.; Grimoldi, A.; Sampietro, M.; Natali, D.; Caironi, M. Printed Photodetectors. *Semicond. Sci. Technol.* **2015**, *30*, 104006.
(29) Liu, X.; Tarn, T.-J.; Huang, F.; Fan, J. Recent Advances in Inkjet Printing Synthesis of Functional Metal Oxides. *Particuology* **2015**, *19*, 1−13.
(30) Ru, C.; Luo, J.; Xie, S.; Sun, Y. A Review of Non-Contact Micro- and Nano-Printing Technologies. *J. Micromech. Microeng.* **2014**, *24*, 053001.
(31) Jang, D.; Kim, D.; Moon, J. Influence of Fluid Physical Properties on Ink-Jet Printability. *Langmuir* **2009**, *25*, 2629−2635.
(32) Vernieuwe, K.; Feys, J.; Cuypers, D.; De Buysser, K. Ink-Jet Printing of Aqueous Inks for Single-Layer Deposition of Al-Doped ZnO Thin Films. *J. Am. Ceram. Soc.* **2016**, *99*, 1353−1359.
(33) Matavž, A.; Frunză, R. C.; Drnovšek, A.; Bobnar, V.; Malič, B. Inkjet Printing of Uniform Dielectric Oxide Structures from Sol−Gel Inks by Adjusting the Solvent Composition. *J. Mater. Chem. C* **2016**, *4*, 5634−5641.
(34) Konstantatos, G.; Badioli, M.; Gaudreau, L.; Osmond, J.; Bernechea, M.; Garcia de Arquer, F. P.; Gatti, F.; Koppens, F. H. Hybrid Graphene-Quantum Dot Phototransistors with Ultrahigh Gain. *Nat. Nanotechnol.* **2012**, *7*, 363−368.
(35) Guo, W.; Xu, S.; Wu, Z.; Wang, N.; Loy, M. M.; Du, S. Oxygen-Assisted Charge Transfer between ZnO Quantum Dots and Graphene. *Small* **2013**, *9*, 3031−3036.
(36) Nian, Q.; Gao, L.; Hu, Y.; Deng, B.; Tang, J.; Cheng, G. J. Graphene/PbS-Quantum Dots/Graphene Sandwich Structures Enabled by Laser Shock Imprinting for High Performance Photodetectors. *ACS Appl. Mater. Interfaces* **2017**, *9*, 44715−44723.
(37) Gong, M.; Sakidja, R.; Liu, Q.; Goul, R.; Ewing, D.; Casper, M.; Stramel, A.; Elliot, A.; Wu, J. Z. Broadband Photodetectors Enabled by Localized Surface Plasmonic Resonance in Doped Iron Pyrite Nanocrystals. *Adv. Opt. Mater.* **2018**, *6*, 1701241.
(38) Liu, Q.; Gong, Y.; Wilt, J. S.; Sakidja, R.; Wu, J. Synchronous Growth of AB-stacked Bilayer Graphene on Cu by Simply Controlling Hydrogen Pressure in CVD Process. *Carbon* **2015**, *93*, 199−206.
(39) Lu, R.; Liu, J.; Luo, H.; Chikan, V.; Wu, J. Z. Graphene/GaSe-Nanosheet Hybrid: Towards High Gain and Fast Photoresponse. *Sci. Rep.* **2016**, *6*, 19161.
(40) Sun, Z.; Liu, Z.; Li, J.; Tai, G. A.; Lau, S. P.; Yan, F. Infrared Photodetectors Based on CVD-Grown Graphene and PbS Quantum Dots with Ultrahigh Responsivity. *Adv. Mater.* **2012**, *24*, 5878−5883.
(41) Wu, J. Z. Graphene. In *Transparent Conductive Materials. Materials, Synthesis and Characterization*; Levy, D., Castellón, E., Eds.; Wiley-VCH: Weinheim, Germany, 2018; Vols. *1, 2*, pp 165−192.
(42) Zhang, D.; Gan, L.; Cao, Y.; Wang, Q.; Qi, L.; Guo, X. Understanding Charge Transfer at PbS-Decorated Graphene Surfaces Toward a Tunable Photosensor. *Adv. Mater.* **2012**, *24*, 2715−2720.
(43) Geim, A. K.; Grigorieva, I. V. Van der Waals Heterostructures. *Nature* **2013**, *499*, 419−425.
(44) Liu, Q.; Gong, M.; Cook, B.; Ewing, D.; Casper, M.; Stramel, A.; Wu, J. Fused Nanojunctions of Electron-Depleted ZnO Nanoparticles for Extraordinary Performance in Ultraviolet Detection. *Adv. Mater. Interfaces* **2017**, *4*, 1601064.
(45) Gong, M.; Sakidja, R.; Goul, R.; Ewing, D.; Casper, M.; Stramel, A.; Elliot, A.; Wu, J. Z. High-Performance All-Inorganic $CsPbCl_3$ Perovskite Nanocrystal Photodetectors with Superior Stability. *ACS Nano* **2019**, *13*, 1772−1783.

DOI: 10.1021/acsanm.9b00539
ACS Appl. Nano Mater. 2019, 2, 3246−3252